Unravelling Heterodyne Force Microscopy

Verbiest, G.J.

CHAPTER 1

General and Experimental Background

In this chapter, we introduce the basic concepts of Atomic Force Microscopy and Heterodyne Force Microscopy. Furthermore, we discus the challenges that we faced and solved, before we could perform Heterodyne Force Microscope experiments. Finally, we discuss the different models, as well as their applicabilities, that are used to describe the tip-sample interaction in Atomic Force Microscopy and Heterodyne Force Microscopy.

1.1 Atomic Force Microscope

The introduction of the Atomic Force Microscope (AFM) in 1986 by Binnig et al. [1] revolutionized surface studies at the nanoscale. The AFM is capable to measure at length scales well below the diffraction limit of optical microscopes. In the past decades, the AFM has developed into a versatile instrument capable of imaging individual atoms at a surface, and it is, by now, unmissable in surface science.

The AFM uses a cantilever to trace height variations of the surface. The cantilever has a sharp tip at its end. The end of the tip is usually regarded as a sphere with a typical radius of 5 nm, which enables the cantilever to sense height variations at the scale of nanometers. Figure 1.1 shows a scheme of a typical AFM setup. The bending of the cantilever is commonly measured via an optical beam (red), which is reflected from the back of the cantilever onto a photodetector. Even a small change in bending of the cantilever, caused by a height variation of the surface, results in a measurable signal on the photodetector (blue). The bending of the cantilever (or force) can be kept constant by a feedback mechanism, which adjusts the z-position of the sample to compensate for a variation in bending. The feedback mechanism is usually a proportional-integral controller (PI controller). The voltage that is necessary to adjust the z-position of the sample provides a measure for the height of the surface. The AFM mode, in which the bending of the cantilever is kept constant, is called contact mode.

AFM operation in contact mode is not the only way to determine the height of the surface. The cantilever of an AFM has typically a first resonance frequency in the range of 1 to 400 kHz. Other AFM modes become available, if the cantilever is excited at or near any of its resonance frequencies. Firstly, in tapping mode or intermittent contact mode, changes in either the amplitude or the phase of the cantilever's response to the excitation frequency can be used as an input for the feedback mechanism. Secondly, in frequency modulation (FM) mode or non-contact AFM, the frequency shift of a chosen resonance frequency is used for the feedback.

All measurements in this thesis were performed with the feedback working in contact mode operation, which is sensitive only to the low frequency (DC part) of the deflection of the cantilever. Although we do not use any resonance frequencies of the cantilever for the feedback, we will see that the shifting of the resonance frequencies plays an important role in the understanding of the results discussed in this thesis. The resonance frequencies shift due to the tip-sample interaction. We will refer to the shifted resonance frequencies as contact resonances.

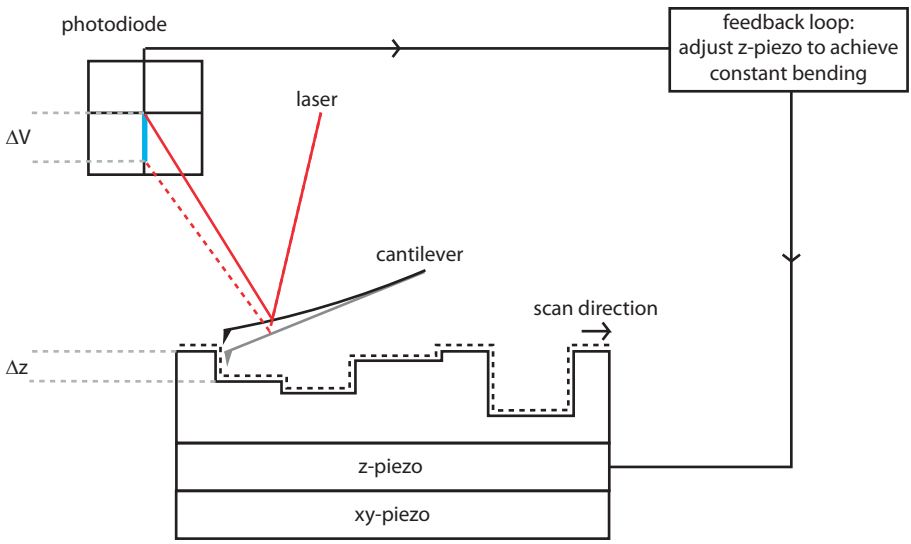

Figure 1.1: Schematics of an AFM setup. The bending of the cantilever is measured via an optical beam method (red). While scanning, the surface is moved in plane using a xy-piezo and the bending of the cantilever is kept constant via a feedback loop. A height change of the surface results in a change in bending of the cantilever, which leads to a different photodiode signal (indicated with the dashed red line and the blue line). The feedback loop instantaneously adjusts the height of the sample via a z-piezo such that the photodiode signal is restored to its original value (adjustable setpoint). The height difference Δz that is necessary to keep the bending of the cantilever constant, is measured from the voltage that is applied to the z-piezo. The feedback uses the photodiode signal ΔV to set the necessary height change Δz. The feedback loop enables the cantilever to follow the height profile of the surface (dashed black line).

1.2 Heterodyne Force Microscope

Heterodyne Force Microscopy has proven to be capable of imaging micro- and even nanoparticles that are embedded significantly deep within the bulk of a sample. To obtain the subsurface information, a HFM setup uses two ultrasonic excitations, one of which is send through the sample (frequency ω_s) and the other through the cantilever (frequency ω_t), see the schematic in Fig. 1.2. Historically, the HFM [2, 3] has been developed on the basis of a combination of an Ultrasonic Force Microscope (UFM) [4], which has been invented in 1993 and is capable of obtaining subsurface information by sending an ultrasonic excitation through the sample only, and a Waveguide Ultrasonic Force Microscope (Waveguide-UFM) [5], which has been invented in 1996 and applies an

ultrasonic excitation only to the cantilever. The unique feature of a HFM with respect to an UFM and a W-UFM is its capability to accurately measure phase shifts between the ultrasonic excitation of the sample and the response of the tip to this. As will be shown in Chap. 2, this provides a more sensitive way to measure subsurface features. The typical frequencies of the applied ultrasounds are in the low MHz regime. The two ultrasonic excitations are chosen such that their frequency difference ($\omega_{\text{diff}} = |\omega_s - \omega_t|$) is below or on the first resonance frequency of the cantilever. Since the tip-sample interaction is *nonlinear*, the high frequency ultrasonic excitations mix and the cantilever experiences a drive force at the low difference frequency, which finally results in a real motion. It is both the amplitude and the phase of this motion at the heterodyne difference frequency that contain the subsurface information.

The first reported HFM measurements showed 'some' subsurface information [3]. Later, a HFM provided images of gold nanoparticles with a diameter

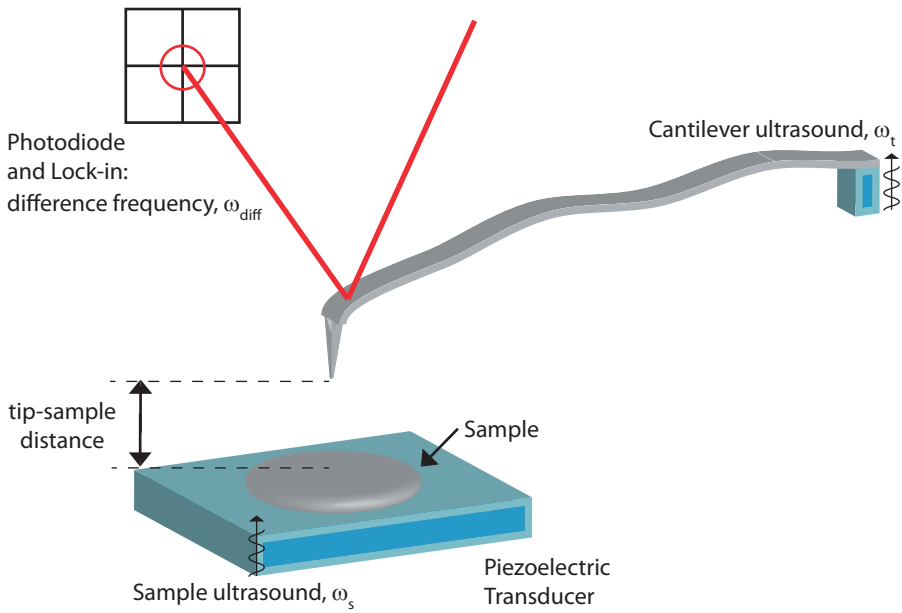

Figure 1.2: Schematic of a HFM setup showing the ultrasonic excitations of the sample (ω_s) and the cantilever (ω_t) as well as the heterodyne, mixed signal at the heterodyne difference frequency (ω_{diff}). A standard AFM setup is used to track the height variations of the surface and to measure the motion of the cantilever at the low heterodyne difference frequency. The detection is accomplished by means of a photodiode.

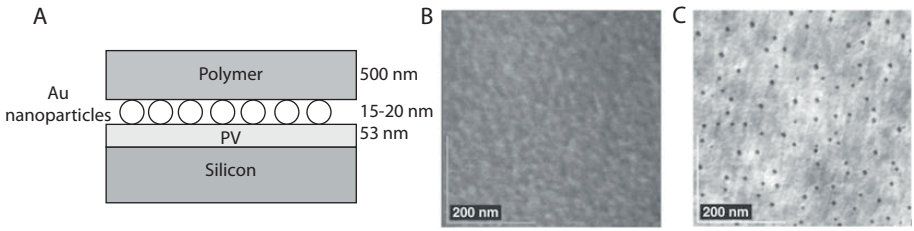

Figure 1.3: Subsurface measurements demonstrating the remarkable contrast and lateral resolution: A) schematic of the sample showing gold nanoparticles with a diameter of $\sim$ 17.5 nm buried at a depth of 500 nm. Both subsurface images were measured simultaneously and they depict the height (B) as well as the phase (C) of the heterodyne difference frequency. Reprinted with permission from [6].

of $\sim$ 17.5 nm buried at a depth of 500 nm (see Fig. 1.3). Figure 1.3B and 1.3C were measured simultaneously and they depict the height as well as the phase of the difference frequency, respectively. The lateral resolution in Fig. 1.3C is remarkable, since it is equal to the diameter of the gold nanoparticles. Considering the wavelength of the ultrasonic excitations, it is hard to understand the reported contrast and resolution. The wavelength of the ultrasonic sample excitation is of the order of mm's, which is much larger than the size of the subsurface nanoparticles (nm's) and their depth below the surface, which is here 500 nm, but can even be up to μm's. As a consequence, the measurement is performed in near-field and one expects the obtainable resolution to be equal to the depth of the nanoparticles. This argument holds only, if the physical contrast mechanism is based on the 'usual' propagation of the ultrasonic wave that is sent into the sample. This brings us to the extreme contrast: the gold nanoparticles are distinct black dots clearly exceeding the variations in the background of the images, although the size of the nanoparticles is only a fraction of the thickness of the sample. Other publications showed subsurface images of equal contrast and resolution [3, 7–15]. None of the reported measurements contain a quantitative analysis of the physical contrast mechanism, which shows that both the contrast and the resolution are not yet understood. It is of great interest to understand these issues, since Heterodyne Force Microscopy has a huge potential for different applications in a wide variety of fields.

In a HFM experiment, one has many ways of choosing the ultrasonic excitation frequencies (including the difference frequency) with respect to the frequency spectrum of the cantilever. As an example, both the ultrasonic tip excitation as well as the excitation at the heterodyne difference frequency can be tuned to coincide with corresponding resonance frequencies of the cantilever, which we call *on-on resonance* excitation scheme. If, on the other hand, the tip

excitation and the heterodyne excitation are both far away of any resonance frequency, we call it *off-off resonance* excitation scheme. Other excitation schemes are *on-off resonance* and *off-on resonance*, in which the first expression refers to the excitation via the low frequency heterodyne signal and the second to the high frequency ultrasonic tip excitation. In the HFM experiments in this thesis, we always have chosen the difference frequency such that it is far below the first resonance frequency of the cantilever. For the ultrasonic tip excitation, we study in Chap. 6 the effects of both the *off-on resonance* and the *off-off resonance* case. As will become clear in this chapter, the different excitation schemes offer different sensitivities to (variations in) the tip-sample interaction and sample properties.

Next to the precise ultrasonic excitation schemes, there are different options to perform the feedback on the height in an HFM experiment. Generally, HFM experiments are carried out in contact mode operation, but also tapping mode operation is reported [13]. In this thesis, we always performed our measurements in contact mode.

1.3 Development of our HFM

Most of the experiments reported were performed on a Nanoscope V Multimode 8 or a Nanoscope III, which are both from Bruker (former Veeco) [16]. During preliminary experiments, we encountered several problems, which prevented us, at this time, from performing a real HFM experiment.

The first problem, discussed in the first subsection, is the electronic crosstalk in the cabling of the AFM between the electronic drive signal of the ultrasonic cantilever excitation and the output of the photodiode.

In the second subsection, we describe why we needed two special piezo elements, with a free resonance of ~ 4 MHz, to excite both the cantilever and the sample ultrasonically.

Finally, the detection of the motion of the cantilever via the standard optical beam deflection method is the cause for the third problem that we encountered. The length of the cantilevers that we typically used, was $\sim 240\,\mu$m. The first resonance frequency of these cantilevers is typically 70 kHz. Each resonance frequency has a certain number of nodes on the cantilever: the first resonance has zero nodes, the second resonance has one node, and so on. The distance between two nodes for the 4^{th} resonance frequency of the cantilever, which is typically 2.6 MHz, is approximately $240\,\mu\text{m}/3.5 = 68\,\mu$m. The diameter of the laser spot size of the Nanoscopes is $\sim 50\,\mu$m. As a consequence, the optical signal at the heterodyne difference frequency is averaged over $50\,\mu$m of the cantilever's local motion. If the spot size of the laser captures the cantilever's motion across a node, this can be problematic, since it will blur especially the phase signal. On a Nanoscope V this results in a phase noise in the order of 1^0. It is possible to reduce this phase noise (even down to the thermal noise of

the cantilever) by measuring on a very special, home-built AFM, which uses a laser with a spot size of only 1 μm [17].

1.3.1 Home-Built Cantilever Holder

The crosstalk in the cabling of the AFM between the electronic drive signal for the ultrasonic excitation of the cantilever and the output of the photodiode was problematic.

The commercially available cantilever holder showed that even *without* a cantilever mounted, the photodiode output produced a significant signal at the electronic drive frequency that should excite the cantilever. To prevent this, we carefully designed a new cantilever holder, which is shielded well enough to prevent the crosstalk and which has, in addition, a second separate piezo element to excite the cantilever at the high ultrasonic frequencies.

Figure 1.4 compares the commercially available cantilever holder with our home-built cantilever holder. The background noise of the photodiode output is shown in gray. We measured the output amplitude of the photodiode as a function of the excitation frequency that is applied to the piezo, which should drive the cantilever at ultrasonic frequencies. We chose the amplitude of the applied electronic drive signal to be always 1 V. The measurements were performed both *with* and *without* a mounted cantilever to receive information on the nature of the crosstalk (electronic vs. mechanical). Panel A compares the photodiode output measured with a mounted cantilever (light blue) and without a mounted cantilever (blue) on the commercially available holder. We observe that only the first two resonance peaks of the cantilever raise over the background signal that is measured without a mounted cantilever. The photodiode output without a mounted cantilever characterizes the electronic crosstalk. Panel B compares the photodiode output measured with a mounted cantilever (light red) and without a mounted cantilever (red) on our home-built cantilever holder. We observe that the resonance peaks clearly exceed the background signal (note that, for low frequencies, the signal between the resonances is even higher than the background measured without a mounted cantilever). Panel C compares the photodiode output measured without a mounted cantilever of both cantilever holders. We clearly see an improvement in the electronic crosstalk for all frequencies. Panel D shows the photodiode output obtained from measurements with a mounted cantilever using the two different holders. To conclude, the home-built cantilever holder has a lower noise level, shows more resonance peaks with an increased amplitude, shows the real transfer function between the resonances, and has a higher signal to noise ratio.

The electronic crosstalk of the commercially available cantilever holder (see Fig. 1.4C) is caused by the cabling inside the AFM itself. The AFM hardware of the Nanoscope III and Nanoscope V is capable of generating an electronic

drive signal for the ultrasonic excitation of the cantilever with a frequency up to 5 MHz. However, mostly, we generated the electronic drive signal with a lock-in externally [18], as it provided us with a larger frequency range, a

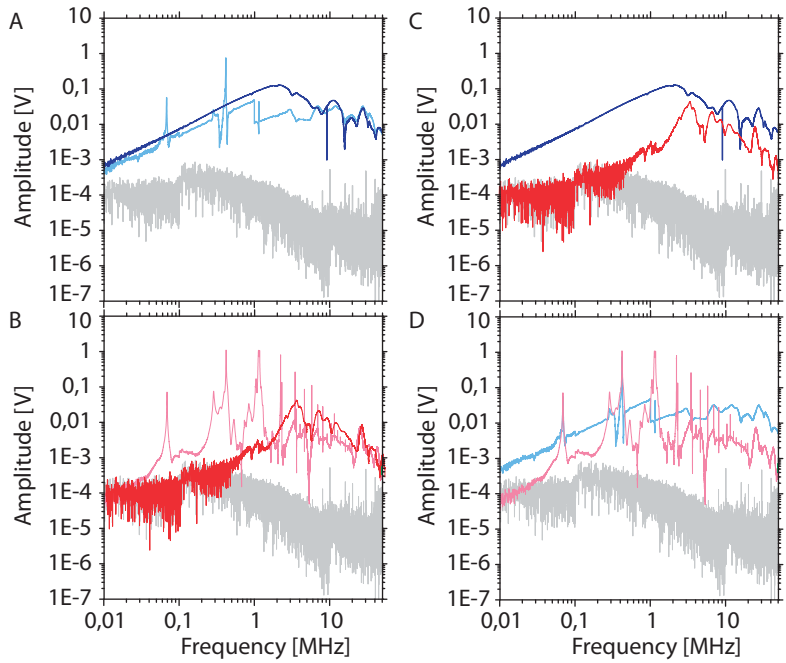

Figure 1.4: Comparison of the commercially available cantilever holder with our home-built cantilever holder. The background noise of the photodiode output is shown in gray. Panel A compares the photodiode output measured with a mounted cantilever (light blue) and without a mounted cantilever (blue) on the commercially available holder. Only the first two resonance peaks of the cantilever raise over the background signal measured without a mounted cantilever. Panel B compares the photodiode output measured with a mounted cantilever (light red) and without a mounted cantilever (red) on our home-built holder. The resonance peaks clearly exceed the background signal (note that, for low frequencies, the signal between the resonances is even higher than the background measured without a mounted cantilever). Panel C compares the photodiode output measured without a mounted cantilever for both holders. We see a clear improvement in the electronic crosstalk. Panel D shows the photodiode output obtained from measurements with a cantilever mounted using the two different holders. The home-built cantilever holder has a lower noise level, shows more resonance peaks with an increased amplitude, shows the real transfer function between the resonances, and has a higher signal to noise ratio.

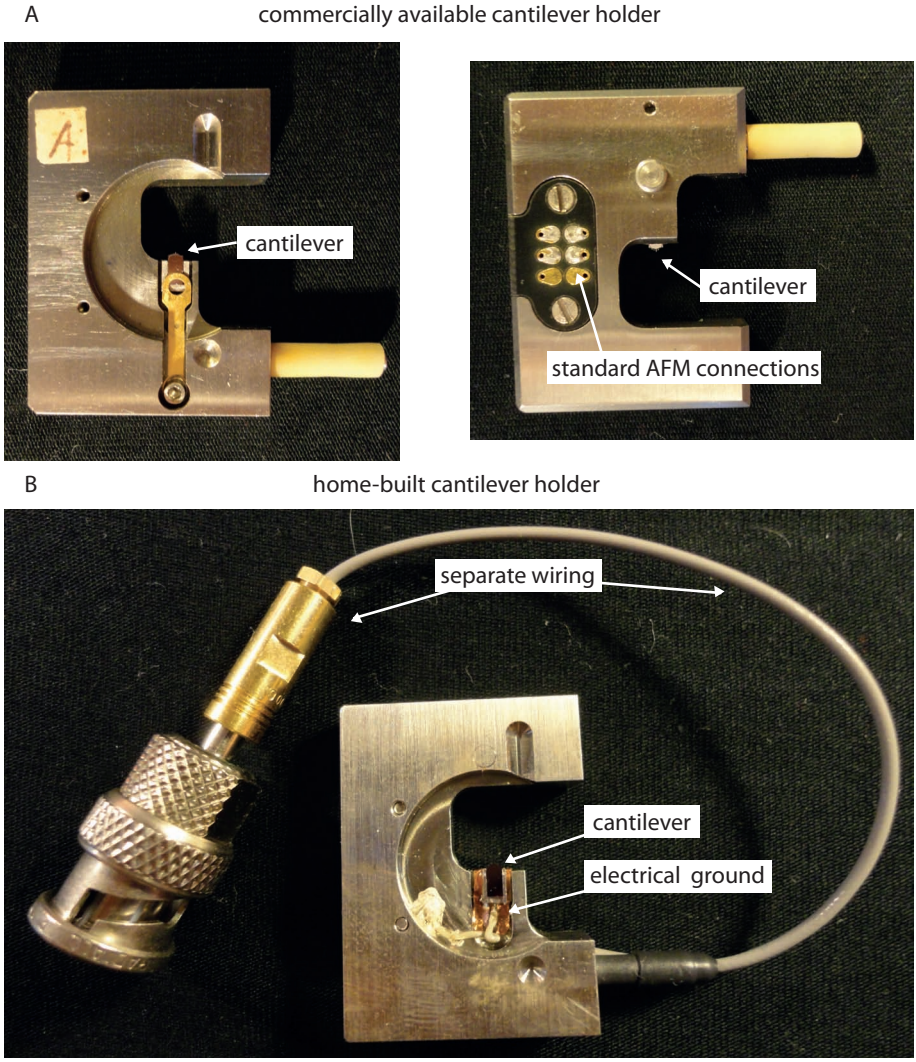

Figure 1.5: The commercially available cantilever holder (A) and the home-built holder (B). In the commercially available holder, the electronic drive signal that excites the piezo underneath the cantilever at ultrasonic frequencies, is sent through the standard AFM connections. In the home-built holder, this electronic drive signal is sent through a completely separate wiring. The electric ground that we added between the piezo elements reduces the electronic crosstalk in the home-built holder.

better time resolution and stability, and more control over the amplitude of

the signal. The externally generated drive signal is hooked up with the microscope via a 'break-out' box. Therefore, the electronic drive signal, is always sent through a cable (located within the base of the scanner), which is part of an inseparable bundle of cables, to the cantilever. This is where the electronic crosstalk manifests itself, as the output of the photodiode is wired through exactly the same bundle of cables. In order to solve this problem, we designed a cantilever holder, of which the electronic drive signal to the cantilever at ultrasonic frequencies is completely separated from the AFM hardware and the standard wiring, see Fig. 1.5.

Our home-built cantilever holder is shown in Fig. 1.6. The complete holder is depicted in (A) and a zoom-in is provided in (B), which shows the individual elements of the designed piezo stack. A cross section through this stack is shown in (C). For our design, we took the following considerations into account. Firstly, we decided to use two separate piezo elements, one of which is used for the ultrasonic excitation of the cantilever and the other for the relatively low-frequency tapping mode operation. Secondly, we wanted to achieve a high as possible resonance frequency of the piezo element that is used for the ultrasonic excitation of the cantilever, which requires to add as little as possible mass from the isolations and the electrodes to this piezo element. Thirdly, isolation plates and an electric ground are necessary to reduce the electronic crosstalk within the entire stack as well as to the ultrasonic piezo element that excites the sample. We decided to use isolation plates made of Al_2O_3 (0.5 mm thick) and special electrodes (0.1 mm thick Cu foil) that have an isolating varnish on one side and that are unvarnished on the other side for electrical connections. Although it might seem, in the following description, that we use the Al_2O_3 plates in a standard way for isolation purposes, the main application of these plates in our design, however, is the reduction of the electronic crosstalk between different electrodes by decreasing the involved capacity due to an increase of the distance between the electrodes. The application of these very special electrodes makes it possible to reduce the total mass of the stack, which is beneficial for the resonance frequencies of both piezo elements. The isolation plates unfortunately do significantly lower the resonance frequencies of both piezo elements, see next subsection. The cantilever (1) is glued on an alignment chip (2), which has an angle such that only the tip touches the sample (and not the whole cantilever), when the sample is approached. Directly assembled below is an Al_2O_3 isolation plate (3) to reduce the electronic crosstalk between the piezo elements that ultrasonically excite the cantilever and the sample, respectively. We use the combination of electrode (4), piezo element (5), and electrode (6) for the ultrasonic excitation of the cantilever. Below the electrode (6), there is an isolation plate (7) and an electric ground (8) to reduce the electronic crosstalk within the entire stack. The electric ground is a very large shield that is at all openings directly connected to the ground/mass of the

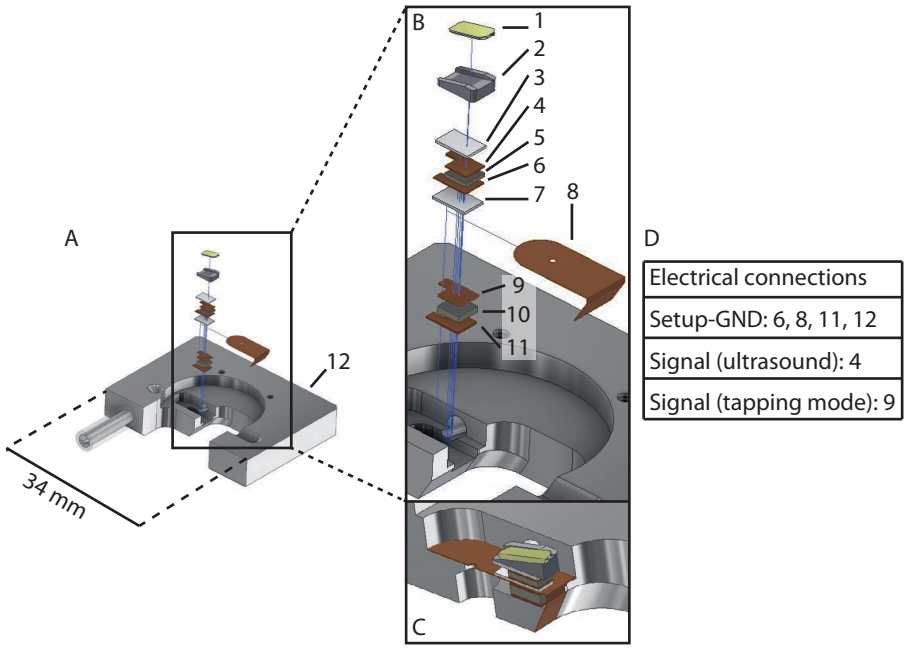

Figure 1.6: The design of our home-built cantilever holder. The complete holder is depicted in (A) and a zoom-in is provided in (B), which shows the individual elements of the piezo stack. A cross section through this stack is shown in (C). We used 0.5 mm thick isolation plates made of Al_2O_3 to reduce the electronic crosstalk between the different elements in the stack as well as to the ultrasonic piezo element that excites the sample. For the electrodes we used 0.1 mm thick Cu foils with an isolating varnish on one side. The cantilever (1) is glued on an alignment chip (2). Directly assembled below is an Al_2O_3 isolation plate (3) to reduce the electronic crosstalk between the piezo elements that ultrasonically excite the cantilever and the sample, respectively. We use the combination of electrode (4), piezo element (5), and electrode (6) for the ultrasonic excitation of the cantilever. Below electrode (6), there is an isolation plate (7) and an electric ground (8) that works like a Faraday cage, to reduce the capacitive coupling and the electronic crosstalk between the two piezos in the stack. We use the combination of electrode (9), piezo element (10), and electrode (11) for normal tapping mode operation. The holder, on which the stack is mounted, is indicated with (12). The electrical connections are indicated in (D).

cantilever holder itself such that it works like a Faraday cage. This completely decouples electronically the upper and the lower piezo element from each other. We use the combination of electrode (9), piezo element (10), and electrode (11) for the usual tapping mode operation with frequencies up to typically 400 kHz

[1]. The holder, on which the stack is mounted, is indicated with (12). The electrical connections are indicated in (D). It is to mention here that the ultrasound attenuation in the Al_2O_3 plates is 1.5 dB/cm for low MHz frequencies. Therefore, if we would use piezo element (10) to apply the ultrasound to the cantilever, 1.7% of the ultrasonic amplitude would be attenuated before the wave reaches the cantilever. For piezo element (5), this is only 0.9%. Although the ultrasound attenuation in the Cu foils is larger ($\sim$ 15 dB/cm), the total thickness of the Cu foils is so small that they attenuate less than 6.7% of the ultrasonic amplitude generated by piezo element (10) and less than 1.7% of the amplitude generated by piezo element (5). As the attenuation of the ultrasonic wave that is generated by piezo element (5) is much less than the wave generated by piezo element (10), we will apply the ultrasound for the cantilever by piezo element (5) and use piezo element (10) for, e.g., tapping mode operation. It is to be expected that the used glue also strongly attenuates the ultrasonic wave, however, as we will see in the next subsection, we obtain a significantly strong transmission of the ultrasound to the cantilever, especially for piezo element (5).

First we glued all electrodes to the piezo elements using a conducting epoxy (Epotek H20E) and a curing afterwards for 1 hour at 120^0C. Then, the complete stack was glued together with a nonconducting epoxy (Epotek H70E) and it was cured afterwards for 1 hour at 90^0C. We applied an external load of $\sim$ 15 N during the gluing/curing process in all of the steps.

During operation we later noticed that the noise could be significantly reduced by connecting the electrode (6) on purpose directly to the ground/mass of the cantilever holder. This 'shortcut' makes the ground of the cantilever holder and the ground of the ultrasonic drive signal exactly the same. The ground of the drive electronics comes, therefore, from the ground of the cantilever holder (without a ground loop being present via the power supplies). Since the piezo element (10) is only operated at relatively low frequencies, we assumed that the combination of electrode (9), piezo element (10), and electrode (11), used for the usual tapping mode operation, was sufficiently isolated from the rest of the holder by the isolating varnish on the electrodes and the application of the nonconducting epoxy.

1.3.2 Ultrasonic Sample and Cantilever Excitation

Figure 1.4A shows (at least for the cantilever) why we needed piezo elements with a free resonance frequency of $\sim$ 4 MHz to excite both the cantilever and the sample ultrasonically. The light blue line represents the response of a mounted cantilever in the commercially available holder to an applied electric drive signal with an amplitude of 1 V. We only see the first two resonance

[1]The Nanoscopes are capable to provide a tapping mode excitation up to $\sim$ 5 MHz.

frequencies of the cantilever at approximately 70 and 450 kHz, respectively. The piezo underneath the cantilever is not capable of exciting the cantilever above 1 MHz. The reason for this is the low resonance frequency ($\sim$ 300 kHz) of this particular piezo element [16].

To solve this problem, we need to use special piezo elements with a free resonance frequency that is higher than (or approximately equal to) the desired ultrasonic tip frequency. Such piezo elements are commercially available from Applied Laser Technology (ALT) [19]. We decided to use piezo elements as characterized in Tab. 1.1 to excite the cantilever and the sample at ultrasonic frequencies. In order to get optimal transmission of the piezo vibrations into both the cantilever and the sample, we directly glued both onto their corresponding piezo elements using Crystalbond 509 [20].

To check whether the first free resonances of the piezo elements are indeed in the order of a few MHz, we measured the voltage V_m in the electric circuit shown in Fig. 1.7A as a function of the frequency. The input voltage V_0 was set to 1 V and we assumed the input resistance R_0 to be zero. The voltage V_m was measured over a resistance, $R_m = 1\,\Omega$, to determine the admittance $Y(\omega)$. The absolute value of the admittance $|Y(\omega)|$ is determined via:

$$Y(\omega) = \left[R_m \frac{V_0}{V_m(\omega)} - (R_0 + R_m) \right]^{-1}.$$

Figure 1.7B shows the absolute value of the admittance $|Y(\omega)|$ as a function of the excitation frequency of the piezo element that will be used to ultrasonically excite the sample. The black line shows the result for the piezo element with both the electrodes and the Al_2O_3 isolation plates mounted on both sides, whereas the red line is measured with only the electrodes (Cu foils). The piezo element with only the Cu electrodes has two resonances below 10 MHz: one at 2.75 MHz and the other at 4.04 MHz. The additional masses of the Al_2O_3 isolation plates lower these resonance frequencies to 2.16 MHz and 3.20 MHz, respectively. Nevertheless, the piezo with the isolation plates still has a resonance frequency above 2 MHz, which is sufficient for our application.

Piezo	dimensions L $\times$ W $\times$ H [mm]	Material
Cantilever	2 $\times$ 2 $\times$ 0.3	PIC 155 [21]
Sample	10 $\times$ 10 $\times$ 0.5	PIC 255 [21]

Table 1.1: The dimensions, length $\times$ width $\times$ height (L $\times$ W $\times$ H), and the materials of the piezo elements that we applied to excite both the cantilever and the sample at ultrasonic frequencies.

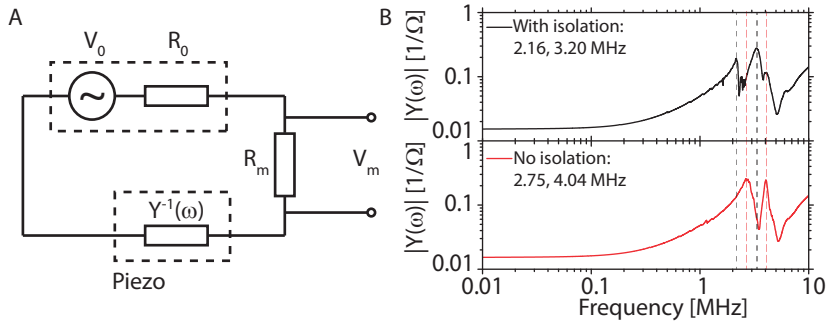

Figure 1.7: The electric circuit used to determine the resonance frequencies of the piezos is shown in (A). The input voltage V_0 is set to 1 V and we assumed the input resistance R_0 to be zero. We measured the voltage V_m over a resistance, $R_m = 1\,\Omega$, to determine the admittance $Y(\omega)$ as a function of the excitation frequency. The absolute value of the admittance $|Y(\omega)|$ of the piezo, as a function of the excitation frequency, is shown in (B). The black line shows the result with both the electrodes and the Al_2O_3 isolation plates mounted on both sides of the piezo elements, whereas the red line is measured with only the electrodes (Cu foils). The vertical dashed lines indicate that the resonance frequencies are shifted towards lower frequencies for the piezo with the Al_2O_3 isolation plates, due to the additional mass of these plates. We still achieve a resonance frequency above 2 MHz.

1.4 Different Models for the Tip-Sample Interaction

The contact, the indentation, and the deformation of two solid objects is a well studied subject that is usually modeled with a sphere pushing into an infinitively large sample with a flat surface. The correct modeling plays an important role in this thesis, as it describes the force (or the interaction) between the cantilever's tip and the sample. We describe this force with the tip-sample interaction F_{ts}, which is a function of the tip-sample distance z. We will see that the precise details (particular form) of the tip-sample interaction significantly determines the cantilever dynamics and, therefore also, the generation of the heterodyne signal. Consequently, we will even demonstrate that variations in the tip-sample interaction lead to a measurable subsurface contrast, although it does not necessarily be related to subsurface features. To provide the necessary background information, we shortly describe five different models and their range of applicability, which depends on both the elastic properties of the tip [2] and the sample as well as on the tip radius R. All models do not

[2] Please note that a proper description takes into account also the elasticity of the cantilever and not only the elasticity of the tip.

take into account any hysteresis or plasticity at high contact forces such that we are also not able to account for these effects in our modeling.

The well-known Hertz model [22] describes the indentation of a sphere into an infinitely large and flat sample at *high* contact forces. In comparison to all other models, the Hertz model does not at all take into account the description of the attractive part of the tip-sample interaction. This implies that for high contact forces all other models should resemble (or should be replaced by) the Hertzian model. The difference between the other models is the exact description of the attractive part of the tip-sample interaction. We will discuss the Bradley model of rigid contact (also called LJ-model, as it is based on a Lennard-Jones potential), the Derjaguin-Muller-Toporov (DMT-) model [23], the Johnson-Kendall-Roberts (JKR-) model [24], and the Maugis-Dugdale (M-D-) model [25].

The LJ-model describes an infinitely hard tip that cannot indent into an infinitely hard sample. The DMT-model is valid for a relatively hard sample, a low surface energy, and a small contact radius, and within this model both the sample and the tip can deform. In the JKR-model, the sample is assumed to be significantly softer than the tip. Furthermore, a large surface energy and large contact radius are required. As a result, the sample deforms under an applied load while the tip does not. The M-D-model is a generalization of the DMT-model and the JKR-model and it has been shown that it is a kind of interpolation between the DMT-model and the JKR-model [25, 26]. Two parameters determine which model is the most appropriate for a certain situation.

An elasticity parameter λ, which is related to the so-called Tabor coefficient μ, determines which of the five models correctly describes the tip-sample interaction. It is also used as the interpolation parameter in the M-D-model indicating the strength of the DMT- and the JKR-model in this description. The elasticity parameter λ and the Tabor coefficient μ are given by:

$$\lambda = 1.16\mu = 1.16 \left[\frac{RH^2}{144\pi^2 E_f^2 a_0^7} \right]^{1/3} \tag{1.1}$$

, in which $H/12\pi a_0^2$ describes the work of adhesion.

The M-D-model is not a 'real' phase between the DMT-model and the JKR-model, but a nonlinear interpolation as a function of λ. For small λ, the contribution of the DMT-model increases and in the case that $\lambda \to 0$, the M-D-model exactly converges to the DMT-model. On the other hand, for large λ, the contribution of the JKR-model dominates and if $\lambda \to \infty$, the M-D-model exactly converges to the JKR-model. $\lambda = 1$ is often treated to be the border between a better description via the DMT- model or a better description via the JKR-model.

In addition to λ, there is also a dependence on the applied load or contact force F_c. The normalized load $\overline{P}$ describes the contact force normalized to the maximum of the adhesion force F_{ad}: $\overline{P} = F_c/|F_{ad}|$.

Taking into account the effects of a variation in $\overline{P}$, which describes the normalized contact force, and the variations in λ, which describes the variation in effective elasticity, it is possible to construct a "phase" diagram, which depicts the applicability of each model as a function of the normalized load $\overline{P}$ and the elasticity parameter λ, see Fig. 1.8.

The simulations and experiments in this thesis were performed with a hard Silicon tip/cantilever pushing into a hard Silicon wafer or into a soft polymer sample. The corresponding areas in the "phase" diagram are depicted in red in Fig. 1.8.

The region between $\lambda = 0.007$ and $\lambda = 0.014$ corresponds to simulations and experiments of a hard Silicon tip/cantilever pushing into a hard Silicon wafer. For these simulations, the diagram shows that both the LJ-model and the DMT-model are applicable depending on the applied contact force. Consequently, we performed the corresponding simulations with tip-sample interactions F_{ts} described by both the LJ- and the DMT-model. Despite the application of the two different models, we do not obtain *any* difference in the results,

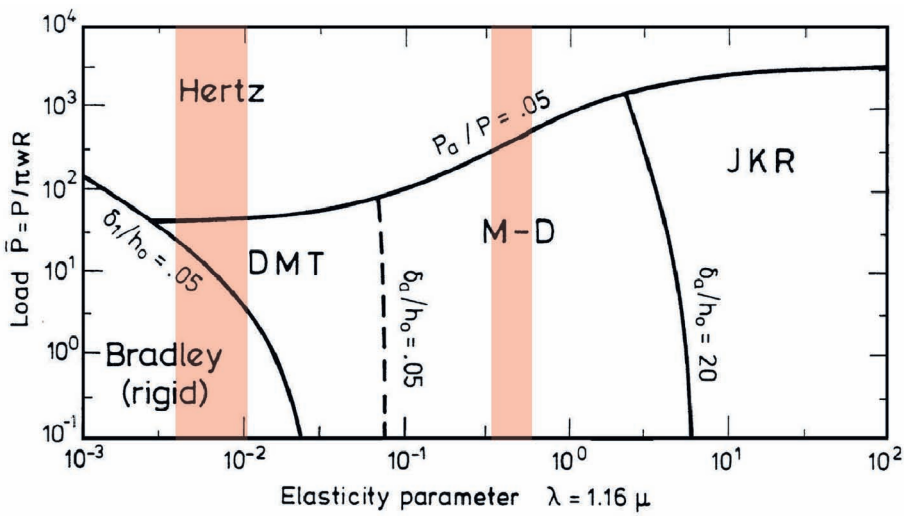

Figure 1.8: "Phase" diagram that indicates the applicability of the different models as a function of the normalized load $\overline{P}$, which describes the normalized contact force, and the elasticity parameter λ, which describes the variation in effective elasticity. The red areas indicate the range of normalized loads $\overline{P}$ and elasticity parameters λ used in our simulations and experiments. Reprinted with permission from [27]

compare the upper with the lower panel in Fig. 4.2. The reason for this is that it does not matter at all for the numerical simulations which of the models describes the tip-sample interaction, as long as the fit perfectly matches the (experimentally obtained) tip-sample interaction. The only thing that matters is the particular shape (form) of $F_{ts}(z)$ and *not* the model that is used to describe this particular interaction. As a consequence, we explicitly would like to mention here that our numerical method is also valid for hard (metal) samples with (gas) voids inside.

The simulations between $\lambda = 0.63$ and $\lambda = 0.85$ describe experiments and the corresponding simulations, in which a hard Silicon tip/cantilever pushes into a soft polymer sample or into a hard Silicon wafer. We obtained the Young's moduli of these samples by fitting the experimentally obtained tip-sample interactions F_{ts} with the DMT-model. As the resulting λ values of these fits are 0.63 and 0.85, one should use the M-D-model. Nevertheless, our approach with the DMT-model is fully justified, since the only thing that matters is the particular shape (form) of $F_{ts}(z)$.

As we only used the LJ-model and the DMT-model in this thesis, we shortly discuss, in the following, the analytical expressions of these two models. In the LJ-model, it is assumed that neither the tip nor the sample can deform under the applied load. If we, in addition, assume a flat sample, the tip-sample interaction is given by:

$$F_{ts}^{LJ}(z) = \frac{2HR}{9a_0^2}\left(\frac{1}{4}\left[\frac{a_0}{z}\right]^8 - \left[\frac{a_0}{z}\right]^2\right) \tag{1.2}$$

, where H is the Hamaker constant, R the tip radius, a_0 is the tip-sample distance, at which the attractive force is maximal, and z is the tip-sample distance. One should use the LJ-model, if both the tip and the sample are very stiff, i.e. small λ with $\lambda \lesssim 0.01$.

The second model that is important within the framework of this thesis, is the DMT-model. In contrast to the LJ-model, the DMT-model has one additional parameter to characterize the tip-sample interaction. This parameter is given by an effective Young's modulus E_f of the tip-sample contact. E_f is a function of the Young's moduli (E_t, E_s) and Poisson ratios (ν_t, ν_s) of the tip and the sample respectively:

$$\frac{1}{E_f} = \frac{1-v_s^2}{E_s} + \frac{1-v_t^2}{E_t}. \tag{1.3}$$

The tip-sample interaction in the DMT-model is given by

$$F_{ts}^{DMT}(z) = \begin{cases} -\dfrac{HR}{6a_0^2} + \dfrac{4}{3}E_f\sqrt{R}(a_0 - z)^{3/2} & \text{, if } z < a_0 \\ -\dfrac{HR}{6z^2} & \text{, if } z \geq a_0 \end{cases} \tag{1.4}$$

Finally, all of these models for the tip-sample interaction do not account for a possible hysteresis in the tip-sample contact, which prevents us from including this effect in our modeling. Hysteresis can arise, e.g., when a water meniscus is formed between the tip and the sample, or when the sample (or the tip) shows (visco)elastic behavior. All hysteresis effects of the mechanical and electrical parts (cantilever, piezo element, lock-in,...) of an HFM scheme could, in principle, be included in our modeling. We will only observe some hysteresis caused by the detection via the lock-in, as described in Chaps. 3 and 4.